HHS Public Access

Author manuscript

*J Nanopart Res*. Author manuscript; available in PMC 2019 May 23.

Published in final edited form as:

*J Nanopart Res*. 2012 May ; 14(5): . doi:10.1007/s11051-012-0861-1.

# Iron oxide nanoparticle synthesis in aqueous and membrane systems for oxidative degradation of trichloroethylene from water

**Minghui Gui**,
Department of Chemical and Materials Engineering, University of Kentucky, Lexington, KY 40506, USA

**Vasile Smuleac**,
Department of Chemical and Materials Engineering, University of Kentucky, Lexington, KY 40506, USA

**Lindell E. Ormsbee**,
Department of Civil Engineering, University of Kentucky, Lexington, KY 40506, USA

**David L. Sedlak**, and
Department of Civil and Environmental Engineering, University of California at Berkeley, Berkeley, CA 94720, USA

**Dibakar Bhattacharyya**
Department of Chemical and Materials Engineering, University of Kentucky, Lexington, KY 40506, USA

## Abstract

The potential for using hydroxyl radical ($OH^{\bullet}$) reactions catalyzed by iron oxide nanoparticles (NPs) to remediate toxic organic compounds was investigated. Iron oxide NPs were synthesized by controlled oxidation of iron NPs prior to their use for contaminant oxidation (by $H_2O_2$ addition) at near-neutral pH values. Cross-linked polyacrylic acid (PAA) functionalized polyvinylidene fluoride (PVDF) microfiltration membranes were prepared by in situ polymerization of acrylic acid inside the membrane pores. Iron and iron oxide NPs (80–100 nm) were directly synthesized in the polymer matrix of PAA/PVDF membranes, which prevented the agglomeration of particles and controlled the particle size. The conversion of iron to iron oxide in aqueous solution with air oxidation was studied based on X-ray diffraction, Mössbauer spectroscopy and BET surface area test methods. Trichloroethylene (TCE) was selected as the model contaminant because of its environmental importance. Degradations of TCE and $H_2O_2$ by NP surface generated $OH^{\bullet}$ were investigated. Depending on the ratio of iron and $H_2O_2$, TCE conversions as high as 100 % (with about 91 % dechlorination) were obtained. TCE dechlorination was also achieved in real groundwater samples with the reactive membranes.

**Electronic supplementary material** The online version of this article (doi:10.1007/s11051-012-0861-1) contains supplementary material, which is available to authorized users.

**Keywords**

Iron oxide nanoparticles; Functionalized membrane; Hydroxyl radical; TCE dechlorination; Hydrogen peroxide; Heterogeneous Fenton

## Introduction

Nanoscale particles have been widely studied in environmental separations and catalytic reactions due to their unique physical and chemical properties (Bell 2003). Their high surface area to volume ratio provides more catalytic sites than bulk particles. In addition, more crystal defects are generated to enhance the catalytic performance via controlled synthesis of nanoparticles (NPs). In the dechlorination of chloro-organics such as trichloroethylene (TCE) and polychlorinated biphenyls (PCBs), iron-based NPs have attracted a growing attention in recent years. They can degrade those toxic compounds effectively by reductive (Wang and Zhang 1997; Zhang 2003; Xu et al. 2005; Savage and Diallo 2005; Tratnyek and Johnson 2006) and/or oxidative pathways depending on the state of iron (Gates and Siegrist 1995; Pignatello et al. 2006; Laine and Cheng 2007).

In reductive dechlorination, zero-valent iron NPs made by borohydride reduction are more effective electron donors than bulk iron. A second metal such as Ni or Pd is usually added to form bimetallic NPs (Fe/Ni or Fe/Pd) with iron, acting as the catalyst of hydrogen generation (Tee et al. 2009). However, both processes lead to the corrosion of iron and formation of iron oxyhydroxide, which lower the activity of iron for reductive type reactions.

In oxidative dechlorination, the heterogeneous Fenton reaction using granular size iron oxides such as goethite, ferrihydrite, hematite, and magnetite activated by $H_2O_2$ has been extensively studied for water remediation (Tyre et al. 1991; Ravikumar and Gurol 1994; Miller and Valentine 1995; Lin and Gurol 1998; Valentine and Wang 1998; Watts et al. 1999; Huang et al. 2001; Yeh et al. 2004; Costa et al. 2008). It takes place on iron oxide surfaces and very little iron is dissolved at near-neutral pH. The hydroxyl radicals ($OH^{\bullet}$) or ferryl ions (Fe[IV]) are formed based on different mechanisms due to the catalysis of iron oxide (Keenan and Sedlak 2008). These oxidants further mineralize various recalcitrant organic contaminants. A recent study (Voinov et al. 2011) further proved that the free radical production in heterogeneous Fenton reaction was primarily attributed to the surface catalysis of iron oxide instead of the dissolved iron ($Fe^{2+}$ or $Fe^{3+}$) released by the particles. The catalytic sites were much more effective than the dissolved ferric ions in the production of $OH^{\bullet}$. The catalytic decomposition of $H_2O_2$ with goethite, ferrihydrite, and hematite has similar surface area normalized rate constants (Valentine and Wang 1998; Huang et al. 2001; Kwan and Voelker 2003). The differences in rate of $H_2O_2$ decomposition are attributed to the specific surface area of iron oxide. Therefore, iron oxide NPs and nanowires with high specific surface area were employed to promote the production of intermediate oxidants from $H_2O_2$ decomposition (Ai et al. 2007; Zelmanov and Semiat 2008; Giraldi et al. 2009; Lewis et al. 2011; Sun and Lemley 2011). To obtain smaller and segregated NPs, different stabilizers (Peng et al. 2006; Guo et al. 2006; He et al. 2007) and supports can be used in the

synthetic process, such as membranes (Xu and Bhattacharyya 2008; Smuleac et al. 2010; Lewis et al. 2011), copolymers (Dhananjeyan et al. 2001), silica, and alumina (Lim et al. 2006; Pham et al. 2009). The recent development of functionalized membrane makes it an ideal platform for NP immobilization. Membrane pores functionalized with polyelectrolytes have ion exchange groups such as carboxylic acids (Hu and Dickson 2007; Singh et al. 2008) and sulfonic acids (Wycisk and Pintauro 1996; Wang et al. 1998), creating a nanoscale polymer matrix inside the pores. Our group also reported the functionalization of polyvinylidene fluoride (PVDF) and polyether sulfone (PES) membranes with polyacrylic acid (PAA) in both organic and aqueous phase for iron NP synthesis (Xu et al. 2005; Xu and Bhattacharyya 2007; Smuleac et al. 2010). However, the direct synthesis and immobilization of iron oxide NPs in the polymeric membranes for water treatment has not been explored.

The objective of this study is to synthesize stabilized iron oxide NPs with high specific surface area in the aqueous phase and inside the membrane pores. Once the iron oxide NPs are immobilized in the PAA functionalized PVDF membranes, the polymer matrix within the pores prevents the particles from aggregation and reduces the particle loss by recapturing the metal ions. TCE was selected as the target contaminant for the oxidative degradation by surface-catalyzed free radical reactions in the presence of $H_2O_2$.

## Experimental section

### Chemicals

All chemicals used in the study were reagent grade without further purification. Sodium borohydride (99.99 %), sodium carboxymethyl cellulose (CMC) (MW = 90,000), titanium oxysulfate (99.99 %), $\gamma$-$Fe_2O_3$ NPs (\50 nm), 1,2-dibromoethane (EDB, 99.5 %), and acrylic acid (99 %) were purchased from Sigma-Aldrich. Hydrogen peroxide (30 wt%), sodium hydroxide (1 M), sulfuric acid (1 M), pentane (99.9 %), ferrous chloride tetrahydrate, and TCE (99.9 %) were obtained from Fisher Scientific. Ethanol (99.5 %) was purchased from Ecros. Potassium persulfate was purchased from EM Science and ethylene glycol (EG) was from Mallinckrodt. Hydrophilized PVDF microfiltration membranes (diameter: 142 mm, thickness: 125 μm, pore size: 0.65 μm, porosity: 70 %) were obtained from Millipore. All of the solutions were prepared by deionized ultrafiltered water (DIUF) from Fisher Scientific. Deoxygenated and DIUF was obtained by purging $N_2$ into DIUF water for 30 min.

### Synthesis of iron oxide NPs

As shown in Fig. 1, CMC-stabilized iron oxide NPs were prepared by controlled oxidation of iron NPs in the aqueous phase. Typically, 0.5 g of CMC was dissolved in 100 mL of deoxygenated and deionized water followed by addition of $FeCl_2$ (0.2 M, 20 mL). $N_2$ was purged for 15 min to promote the formation of $Fe^{2+}$–CMC complex (He and Zhao 2008). 50 mL of $NaBH_4$ (0.2 M) was then added into this precursor solution dropwise (5 mL/min) and the black iron NPs were formed immediately (Wang and Zhang 1997). After $NaBH_4$ was consumed, the compressed air was bubbled into the solution at a flow rate of 40 mL/min. The solution turned brown due to the oxidation. To stop the oxidation, the particles were

centrifuged and washed with ethanol twice. After washing, the particles were redistributed in ethanol and dried in the oven at 90° C.

### Functionalization of PVDF membranes with PAA

PVDF membranes were functionalized by PAA which was formed via in situ polymerization of acrylic acid (Smuleac et al. 2010). The polymerization solution was composed of monomer acrylic acid (10 mL), initiator potassium persulfate (0.77 g), cross-linker EG (0.5 mL), and deoxygenated and deionized water (40 mL). PVDF membranes were dipped into this solution for 5 min and sandwiched between two glass plates. Then the plates were put into the oven at 90° C for 4 h. $N_2$ was purged into the oven to remove $O_2$ and protect the polymerization of acrylic acid. Due to the thermal treatment, cross linked PAA chains were formed inside the PVDF membrane pores. After the functionalization, the membranes were washed with DIUF water and soaked in ethanol for 12 h to dissolve the unreacted monomers and byproducts.

### Synthesis of iron oxide NPs in PAA/PVDF membranes

PAA/PVDF membranes (diameter: 4.7 cm) were dipped in 200 mL of NaOH solution (pH 9.5–10) to convert the carboxyl groups (−COOH) on PAA chains into −COONa. NaCl (68.4 mM) was added to enhance the ion exchange process. After 12 h, the membranes were washed with DIUF water until the pH of washing solution became neutral. Then they were immersed in 200 mL of $FeCl_2$ solution (3.57 mM) at pH 5–5.3 for 4 h to capture $Fe^{2+}$ by cation exchange. Each ferrous ion was associated with two carboxyl groups and $Na^+$ was released from the membranes. $N_2$ was bubbled to prevent the oxidation of $Fe^{2+}$. After the ion exchange, the membranes were immersed in 50 mL of $NaBH_4$ (264 mM), which reduced $Fe^{2+}$ to $Fe^0$. The membranes turned black and generated $H_2$ immediately. Following the reductive treatment, compressed air was purged into the solution at the flow rate of 20 mL/min. The membranes turned brown after the oxidation and were stored in ethanol after washing with deoxygenated and deionized water.

### Characterization of NPs and membranes

The hydrodynamic diameters and zeta-potentials of particles were determined using dynamic light scattering (DLS) and electrophoretic light scattering (ELS) within a Delsa™Nano submicron particle size and zeta potential analyzer. Brunauer–Emmett–Teller (BET) surface areas of iron and iron oxide NPs were determined using $N_2$ physisorption in a Micromeritics TriStar 3000 surface area and pore size analyzer. The samples were degassed in $N_2$ overnight at 120° C before the analysis. The analytical error was <7 %.

A Hitachi S4300 Scanning Electron Microscopy (SEM) and a JEOL 2010F Transmission Electron Microscopy (TEM) coupled with energy dispersive X-ray spectrometer (EDX) were used to observe the NP morphology and analyze the elemental composition. The membrane cross-sectional samples for SEM were obtained via freezing and fracturing the membrane in liquid $N_2$.

Mössbauer spectroscopy with $^{57}Co$ $\gamma$-ray radiation and X-ray photoelectron spectroscopy (XPS) employing a Kratos XSAM 800 surface analysis system with Mg-K$\alpha$ (1253.6 eV)

radiation were used to identify the oxidation state and surface composition of iron oxide NPs.

X-Ray diffraction (XRD) analysis was performed with Cu-Ka (1.5418Å) radiation using a Bruker-AXS D8 Discovery diffractometer to detect the material crystallography. Fourier transform infrared spectroscopy (FTIR) with attenuated total reflectance (ATR) was used to verify the coating of CMC on iron oxide surfaces as well as the interaction between PAA and iron oxide NPs inside the membranes. The membranes were dried in the vacuum oven at 40° C before the test. Data were collected using 128 scans at a resolution of 4 $cm^{-1}$.

The amount of iron immobilized in the membranes was determined from a material balance of $Fe^{2+}/Fe^{3+}$. The concentration of $Fe^{2+}/Fe^{3+}$ in the feed solution and after the ion exchange was measured by Varian SpectrAA 220 Fast Sequential atomic absorption spectrometer (AAS) with a Fe lamp operated at the wavelength of 386.0 nm. The analytical error was <5 %. The result was checked by digesting the membrane in nitric acid (40 mL, 35 wt%), followed by the measurement of iron concentration with AAS and inductively coupled plasma atomic emission spectroscopy (ICP-AES). The amount of iron oxide dissolved in the reaction was determined by filtering the solution through the regenerate cellulose ultrafiltration membrane (NMWL10000, Millipore) and detecting the iron concentration in the filtrate.

## Oxidative dechlorination of TCE

All of the experiments were carried out at 25° C in 20 mL EPA glass vials. The pH of samples was adjusted to 6.95–7.00 by NaOH (0.1 M) and $H_2SO_4$ (0.1 M) before the reaction and measured throughout the reaction. Iron oxide NPs were sonicated in 15 mL of DIUF water for 30 s. Then 5 mL of TCE (1.08 mM) and 85 μL of $H_2O_2$ (9.75 M) were added into the vial which was wrapped with the lightproof paper and put in a shaker (300 rpm). Pentane was used to extract TCE from the solution and 1,2-dibromoethane (EDB) was used as an internal standard. Typically, 2 mL of sample was mixed with 2 mL of EDB/pentane standard solution for 30 min to achieve the extraction equilibrium. Two control groups without adding $H_2O_2$ or catalyst were used to quantify the loss of TCE due to volatilization and $H_2O_2$ auto-decomposition.

The concentration of TCE was analyzed by HP 5890 Series II GC–MS with a 60 m × 0.25 mm × 14 μm film thickness Supelco SPB624 fused silica capillary column. The calibration curve was obtained via plotting the peak area ratios between TCE and EDB with the concentrations of TCE from 0.0270 to 0.270 mM ($R^2$ = 0.997). The average analytical error was <7 %.

## Degradation of $H_2O_2$

In TCE oxidation, samples were taken out of the vials at regular intervals and filtered through 0.45 μm PVDF autovial syringeless filters (Whatman). The concentrations of $H_2O_2$ were analyzed by Varian Cary Bio300 UV–Visible absorption spectroscopy with the detection at 407 nm ($R^2$ = 0.995). Titanium oxysul-fate was added as the indicator (10 μL/1 mL sample) (Clapp et al. 1989). The analytical error was <3 %.

### Chloride ion analysis

If TCE was completely oxidized by free radicals, the C–Cl bond would be broken and $Cl^-$ would be released to the solution. The amount of chloride formed in the oxidation was measured using an Orion Chloride Electrode (Thermo). The calibration curve was obtained by diluting the chloride standard (Thermo Orion, 2.82 mM) with DIUF water and plotting the electrode potentials $E$ (mV) as a function of log[$Cl^-$]. Based on the Nernst equation, $E$ has a linear relationship with log[$Cl^-$] ($R^2$ = 0.994). The average analytical error was <5 %. 2 % (volume) of sodium nitrate (LabChem Inc., 5 M) was added into the samples as the ionic strength adjusters (ISA) which ensured that the samples had similar ionic strength. The results were checked by adding an aliquot of chloride standard to the sample. From the potentials after the addition, the chloride concentration in original samples could be determined.

## Results and discussions

### Properties of iron and iron oxide NPs

SEM images show that the size of CMC-stabilized iron oxide NPs is between 20 and 30 nm (Fig. 2a). DLS gives a larger $z$-average diameter of 76 nm due to the agglomeration of particles (Fig. S1 of Supplementary material). The Mössbauer spectra of iron NPs before (Fig. 2b) and after oxidation (Fig. 2c) prove that $Fe^0$ made in the aqueous phase has a core–shell structure which is formed by a pure iron core and an iron oxide shell (Nurmi et al. 2005). The Fe–B alloy compound was also observed due to the oxidation of boron. The thickness of shell increases and finally the iron core disappears during the air oxidation in water. The base particle size of iron (Fig. 3a) observed under the high-resolution TEM images (HRTEM) was <10 nm. After oxidation, iron oxide NPs aggregated and exhibited irregular shapes (Fig. 3b), but they could be identified by EDX and selected area electron diffraction (SAED). EDX shows that the atomic ratio of oxygen and iron (O/Fe) increases from 1.07 to 1.94 during the oxidation (Fig. 3c, d). SAED pattern coincided with the diffraction pattern of two-line ferrihydrite (Miller indices: 110 and 300; $d$-spacing: 0.252, 0.151 nm). BET surface area of iron NPs was 37.8 $m^2/g$ (Fig. S2a in Supplementary material). It increased during the air oxidation (Fig. S2b in Supplementary material) and went to 253.4 $m^2/g$ after 2 h (Fig. S2c in Supplementary material). The high specific surface area might be due to the highly porous surface of iron oxide formed by oxidation of iron. Nonporous $\gamma$-$Fe_2O_3$ NPs were used as a control to verify the pores formed in iron oxidation (Fig. S2d in Supplementary material). XPS (Fig. S3a–c in Supplementary material) of iron oxide NPs also verifies that $Fe^0$ is converted to ferric oxide after air oxidation. XRD spectra show the diffraction patterns of iron and iron oxide particles (Fig. 4). The freshly made $Fe^0$ is composed of α-Fe crystals (Fig. 4a) while the shell transfers to two-line ferrihydrite during the oxidation (Fig. 4b–d). These findings coincided with the TEM results. When the oxidation time increased, some other oxide phases such as goethite and lepidocrocite might be formed as indicated by new peaks in the XRD patterns (Fig. 4d) (Furukawa et al. 2002; Hwang et al. 2010). $Fe^0$ aged for 120 days in a sealed 20 mL vial (Fig. 4e) had both α-Fe and iron oxide characteristic peaks, which originated from a core–shell structure.

The size of iron and iron oxide particles calculated from XRD patterns by Scherrer's formula was 7.8 and 3.1 nm, which were consistent with the base particle size. ATR–FTIR spectrum of CMC-stabilized iron oxide NPs (Fig. 5b) shows that the O–H stretching is shifted significantly and the asymmetric $CH_2$ stretching is missing compared with pure CMC (Fig. 5a). Both of them indicate that an enhanced intermolecular hydrogen bond was formed between CMC and the particle surfaces (He et al. 2007). The centrifugation after the particle synthesis removes CMC in the bulk solution, but a thin layer of CMC is adsorbed on the particle surfaces through H-bonding.

During the iron synthesis, the pH of solution is lower than the point of zero charge (PZC) of iron ($pH_{PZC}$ = 7.80) (Kanel et al. 2005). Hence, the particle surface exhibits a positive charge. The negatively charged CMC coating tends to bind the surface of $Fe^0$ and stop the growth of iron NPs as well as preventing them from agglomeration. Figure S4 in Supplementary material shows the zeta-potential of $Fe^0$ prepared with CMC and without CMC. After introducing CMC in the particle synthesis, PZC of $Fe^0$ decreased from 8.10 to 7.70. This again proved that CMC was coated on the particle surfaces and the coating neutralized the surface positive charge, making the particles more stable.

To understand the effects of oxidation on iron, CMC-coated iron NPs were aged at 25° C in a sealed vial containing 20 mL of air. When the particles are oxidized in the aqueous phase, some iron oxides such as ferrihydrite are formed on the particle surface. The PZC of natural ferrihydrite is between 5.30 and 7.50 (Schwertmann and Fechter 1982) while the freshly made and Si-free ferrihydrite is around 7.60 (Saleh and Jones 1984), which is close to that of $Fe^0$. Therefore, CMC will stay on the surface of ferrihydrite during the oxidation. After 120 days, the PZC of the aged particles was 7.05. The significant change of PZC shows that new substances are formed near the surface and they have a reduced surface charge, which could be explained by the formation of an iron oxide shell.

## Degradation kinetics of $H_2O_2$ with iron oxide NPs in the aqueous phase

The Fenton's reagent in acidic pH conditions (pH 3) has been extensively studied due to its applicability in various water related applications. $OH^{\bullet}$ are produced via the reaction of ferrous(II) ions with $H_2O_2$. The ferric(III) ions are formed in the process and reduced by perhydroxyl radicals ($HO_2^{\bullet}$) to regenerate the ferrous(II) ions (Fenton 1894). As a powerful and indiscriminate oxidant, $OH^{\bullet}$ can oxidize most organic contaminants (Pignatello et al. 2006). The concentration of $OH^{\bullet}$ in water is very low ($10^{-6}$–$10^{-4}$ M) due to its high reactivity with most organics ($k = 10^7$–$10^{10}$ $M^{-1}$ $s^{-1}$).

However, it is not practical to conduct the water remediation at low pH. Various methods have been reported to extend the useful pH range to the neutral conditions. The nontoxic iron-chelating agents such as citrate (Li et al. 2007b; Lewis et al. 2009), gluconic acid (Ahuja et al. 2007), and phosphotungstate (Lee and Sedlak 2009) have been used to bind ferrous and ferric ions. The other way is switching to the heterogeneous Fenton reaction using iron oxides (in NPs form) activated by $H_2O_2$.

The decomposition of $H_2O_2$ catalyzed by iron oxide is a pH-dependent process which is primarily based on a modified Haber–Weiss mechanism (Kitajima et al. 1978; Lin and Gurol 1998).

$$\equiv \mathrm{Fe(II)} + H_2O_2 \rightarrow \equiv \mathrm{Fe(III)} + OH^- + OH^{\bullet} \quad (1)$$

$$\equiv \mathrm{Fe(III)} + H_2O_2 \rightarrow \equiv \mathrm{Fe(II)} + H^+ + HO_2^{\bullet} \quad (2)$$

$$H_2O_2 + OH^{\bullet} \rightarrow H_2O + HO_2^{\bullet}, \quad (3)$$

where ≡Fe(II) and ≡Fe(III) stand for iron oxide surfaces. At the neutral pH, it has been established that $H_2O_2$ decomposition in the presence of iron oxide can often be described by pseudo-first-order reaction:

$$-\frac{dC_{H_2O_2}}{dt} = k_{obs}C_{H_2O_2}, \quad (4)$$

where $C_{H2O2}$ is the concentration of $H_2O_2$ in the aqueous phase at the time $t$ and $k_{obs}$ is the observed first-order reaction rate of $H_2O_2$ which depends upon the type of iron oxide present as well as the solution conditions such as pH and temperature. In the absence of TCE, $C_{H2O2}$ obtained in the reaction with different loadings of iron oxide NPs fit the pseudo-first-order approximation. The $k_{obs}$ values for $H_2O_2$ decomposition were 0.0170 $h^{-1}$ (iron oxide loading: 0.67 g/L) and 0.0421 $h^{-1}$ (iron oxide loading: 1.33 g/L) (Fig. 6b). The reaction was initiated when $H_2O_2$ arrived at iron oxide surfaces. Hence, Equation (4) can be written as:

$$-\frac{dC_{H_2O_2}}{dt} = k_{SA}\rho_m a_S C_{H_2O_2}, \quad (5)$$

where $a_S$ is the specific surface area of NPs, $p_m$ is the loading of NPs in the system, and $k_{SA}$ is the surface area-normalized rate for $H_2O_2$ decomposition. Therefore, the estimated $k_{SA}$ values are $1.46 \times 10^{-4}$ L/(h $m^2$) and $1.80 \times 10^{-4}$ L/(h $m^2$), which are quite similar for different loadings of particles. This result supports the conclusion that $H_2O_2$ decomposition with iron oxides is a surface-initiated reaction and a high surface area to volume ratio will enhance the reactivity. The dissolved iron concentration never exceeded 60 μM. Blank $H_2O_2$ and silica/$H_2O_2$ solutions were used as the control groups. Less than 2 % of $H_2O_2$ was lost via auto-decomposition for both groups.

### Catalytic oxidation of TCE with $H_2O_2$ and iron oxide NPs in the aqueous phase

TCE (0.270 mM) was oxidized in iron oxide (1.33 g/L)/$H_2O_2$ (41.4 mM) system and the conversion achieved 98.3 % after 24 h (Fig. 6a). The consumption of $H_2O_2$ was 83.7 %. The pH of solution dropped to 4.60 from 6.95. TCE degradation rate maintained as its concentration decreased. This result was consistent with the previous report of phenol oxidation (Miller and Valentine 1999; Pham et al. 2009). The control group shows that the concentration of TCE decreases by ~6 % due to the volatilization. The auto-decomposition of $H_2O_2$ without the catalysis of iron oxide also led to <2 % of TCE oxidation in the control group. The result indicates the formation of highly oxidative intermediates during the reaction as TCE degradation was not observed unless both iron oxide NPs and $H_2O_2$ appeared in the solution.

The final oxidation products of TCE are expected to be chloride ions ($Cl^-$), organic acids, and carbon dioxide. Three moles of $Cl^-$ should be formed for completely oxidizing 1 mol of TCE. Therefore, the concentrations of $Cl^-$ were analyzed to assess the oxidation efficiency. The yield of $Cl^-$ ($[Cl^-]_{obtained}/[Cl^-]_{max}$) was 80.7 % after 24 h and 91.5 % after 48 h (Fig. 7a). As each mole of TCE was oxidized, 2.74 mol of $Cl^-$ was detected in solution (Fig. 7b). The amount of $Cl^-$ formed and TCE destructed both approached the maximum values, and their ratio ([$Cl^-$-formed]/[TCE oxidized]) increased during the reaction (Fig. 8). This could be explained by the formation of chlorinated intermediates and the release of $Cl^-$-from TCE step by step. Generally, TCE oxidation by $OH^\bullet$ forms chloroacetic acids, which were further oxidized by $OH^\bullet$ and finally degraded into hydrochloric acid, formic acid, and carbon dioxide (Watts and Teel 2005; Huling and Pivetz 2006; Pignatello et al. 2006; Li et al. 2007a; Lewis et al. 2009).

When the loading of particles was halved (0.67 g/L), the conversion of TCE was 74.7 % after 24 h (Fig. 6a). The total consumption of $H_2O_2$ was reduced by 45.6 % (Fig. 6b). The yield of $Cl^-$ was 80.5 % after 24 h and 83.2 % after 48 h. Therefore, as each mole of TCE was degraded, 2.50 mol of $Cl^-$ was detected in solution.

$H_2O_2$ decomposition before and after adding TCE is shown in Fig. 6b. The results indicate that the rate of $H_2O_2$ decomposition was nearly unaffected by introducing TCE to the system. Most $OH^\bullet$ were quenched by $H_2O_2$ and free radicals although these parallel reaction rates were relatively low or in the same order of magnitude as that of TCE with $OH^\bullet$ ($k = 4\times10^9\ M^{-1}\ s^{-1}$).

Iron oxide NPs were dissolved in nitric acid (35 wt%) and the concentration of iron was analyzed by AAS. The result shows that each milligram of iron oxide contains 0.49 mg of iron.

### Efficiency of heterogeneous Fenton reaction

The efficiency of $H_2O_2$ use for TCE oxidation can be defined as the amount of TCE degraded per mole of $H_2O_2$ consumed.

$$E = \frac{\Delta\,[\mathrm{TCE}]}{\Delta\,[\mathrm{H_2O_2}]} \times 100\% \quad (6)$$

In this study, $E = 1.21 \pm 0.19$ % for CMC-stabilized iron oxide NPs. The efficiency of iron oxide/$H_2O_2$ system has been reported to be between 0.100 and 0.948 % in the mineralization of quinoline (Valentine and Wang 1998) and phenol (Pham et al. 2009), depending on the ratio of model compounds and $H_2O_2$. The low efficiency could be explained by the decomposition of $H_2O_2$ into $H_2O$ and $O_2$ based on the non-radical electron transfer mechanism (Lee et al. 2001; Pham et al. 2009). The formation of ferryl ions (≡Fe[IV]) may also decrease the production of $OH^{\bullet}$. Ferryl ions were less reactive than $OH^{\bullet}$ and might be unable to decompose the compounds with high energy bonds. Alternatively, $OH^{\bullet}$ could be quenched by reacting with $H_2O_2$ and other free radicals. The potential scavenging effect of $OH^{\bullet}$ by iron oxide surfaces was another possible explanation (Xue et al. 2009).

## Reuse of iron oxide NPs

After the first cycle, the particles were collected, washed with ethanol, and dried in the oven at 90° C. They were sonicated and reused in TCE oxidation (1.33 g/L). The same amount of TCE (0.270 mM) and $H_2O_2$ (41.4 mM) was added. After 24 h, the conversion of TCE was 98.0 %. However, the consumption of $H_2O_2$ increased to 99.7 %. Hence, the efficiency went down to 0.740 ± 0.09 %. The yield of $Cl^-$ was 73.9 % (i.e., 2.22 mol of $Cl^-$ were obtained as each mole of TCE was oxidized). In the surface-catalyzed reaction, iron oxide existed in the forms of ≡Fe(III) and ≡Fe(II) which were interconverted by reacting with $H_2O_2$. Ferric oxyhydroxide could be formed due to the precipitation of $Fe^{2+}/Fe^{3+}$ released from particles. The components of iron oxide might change during the catalytic reaction, which affected the specific surface area of particles or the number of catalytic sites. BET surface area test shows that the specific surface area of iron oxide NPs decreases from 175.5 to 142.0 $m^2/g$ after TCE oxidation. The particles could also aggregate due to the degradation of CMC coating. Therefore, the change of particle size and composition led to the decline of efficiency.

## Properties of PAA/PVDF membranes immobilizing iron oxide NPs

The PVDF microfiltration membranes were used as a support for iron oxide NP synthesis due to its high resistance to most solvents and heat. When PVDF was modified by in situ polymerization of acrylic acid, cross-linked PAA was created inside the pores and it provided the free carboxyl groups for ion exchange (Fig. 9). $Fe^{2+}$ was introduced to the polymer chains via electrostatic bonding with carboxyl groups. The environmental pH must be above the p*K*a value of PAA (4.30–4.90) during ion exchange to maintain the carboxyl groups in their dissociated state (Hu and Dickson 2007). To prevent the pH drop during direct $Fe^{2+}$ capture, the membranes (Fig. 9a) were preloaded with $Na^+$. Both iron (Fig. 9b) and iron oxide ((Fig. 9c, d) NPs were formed inside the membrane pores. AAS and ICP-AES show that all of the iron picked up by PAA chains in ion exchange is converted into iron oxide NPs (Table S1 in Supplementary material). The atomic ratio of $Na^+$ released from the membranes over $Fe^{2+}$ bound to the membranes is 1.9 ± 0.05.

A small amount of NPs were also formed on the surface of PAA/PVDF membranes due to the physical sorption of ferrous ions during ion exchange. The resulting particles aggregated with each other on the membrane surface (Fig. 10a) while spreading uniformly in the pores (Fig. 10b). This verifies that the polymer matrix inside the membrane pores can prevent the agglomeration of particles effectively. SEM images of membrane cross-section samples show that the size of particles after air oxidation for 1 h is between 80 and 100 nm (Fig. 10c). However, the spherical iron oxide NPs are transformed into nanoscale aggregates after TCE oxidation (Fig. 10d), which may be hydroxide precipitates of $Fe^{2+}/Fe^{3+}$ released by the particles. ATR–FTIR spectrum of PAA functionalized PVDF membranes shows a peak at 1,710 $cm^{-1}$, which is from the C=O bond stretching in carboxyl groups (Fig. 11b). This peak indicates the existence of cross linked PAA in PVDF membranes. When iron oxide NPs are immobilized in the membranes, this peak shifts to 1,560 $cm^{-1}$ due to the interaction between PAA and particles (Fig. 11c). The strong C–F bond stretching from PVDF is shown at 1,000–1,360 $cm^{-1}$ and does not shift during the membrane functionalization and particle formation (Fig. 11a). This proves that PVDF is a stable support for thermal and chemical treatment.

## Catalytic oxidation of TCE with $H_2O_2$ in the iron oxide/PAA/PVDF membrane system

TCE (0.270 mM) was oxidized in the catalytic membrane system which was activated by $H_2O_2$ (41.4 mM). The total iron loading in the membrane is 0.88 g/L as iron oxide NPs. After 48 h, the concentration of TCE decreased by 74.7 % (Fig. 12). The degradation rate of TCE appeared constant during the reaction as observed in the experiment using CMC-stabilized iron oxide. The conversion of $H_2O_2$ was 86.6 % after 24 h, and 96.7 % after 48 h. $H_2O_2$ decay was in agreement with pseudo-first-order kinetics and $k_{obs}$ = 0.0842 $h^{-1}$. The pH of solution was 6.80 after 48 h. Less than 20 μM of iron was dissolved in the solution. The yield of $Cl^-$ was 40.9 % and the overall [$Cl^-$ formed]/[TCE degraded] was 1.23 (Figs. 13, 14). This indicates that not all C–Cl bonds in TCE are broken or $Cl^-$ prefers to stay in the polymer matrix. The efficiency is 0.36 ± 0.08 %, which indicates that 280 mol of $H_2O_2$ is necessary to decompose each mole of TCE.

Blank PAA/PVDF membranes were mixed with TCE and $H_2O_2$ to determine the loss of TCE due to the membrane extraction. About 0.04 mM of TCE was extracted by the membranes. The amount of $H_2O_2$ decreased was within 3 % of its initial value. $H_2O_2$ decay with only iron oxide/PAA/PVDF membranes also fit the first-order kinetics and the presence of TCE had little effect on $H_2O_2$ decomposition.

## Reuse of iron oxide/PAA/PVDF membranes

The membranes were washed with deoxygenated and deionized water after the experiment and dried in vacuum oven at 40° C for the second cycle test. The same amount of TCE (0.270 mM) and $H_2O_2$ (41.4 mM) was added. After 48 h, the conversion of TCE was 60.4 % and the consumption of $H_2O_2$ increased to 98.4 %. The efficiency went down to 0.320 ± 0.07 %, and the yield of $Cl^-$ was 38.9 %.

### TCE oxidation with iron oxide/PAA/PVDF membranes in real groundwater samples

To demonstrate that the catalytic membranes could be used in the treatment of contaminated groundwater, a batch experiment was carried out using the real groundwater taken from the Paducah Gaseous Diffusion Plant Superfund Site in western Kentucky. The groundwater sample (pH 7.4–7.5) contained a small amount of $Fe^{2+}/Fe^{3+}$ (5.36 μM), $Ca^{2+}$ (600 μM), and $Cl^{-}$ (1.55 mM). After 33 h, the conversion of TCE (0.270 mM) was 53.5 % while 93.4 % of $H_2O_2$ (41.4 mM) was consumed. The yield of $Cl^{-}$ was 66.7 % and the efficiency was 0.220 ± 0.07 %. The iron loading as iron oxide NPs in the membrane system was 0.435 g/L.

### Comparison of iron oxide NPs and iron oxide/PAA/PVDF membranes

Iron oxide NPs in the aqueous phase and membrane system show promising application in water remediation. Complete degradation of TCE could be obtained via $H_2O_2$ addition, depending on the amount of catalyst and $H_2O_2$ in the system. The diffusivity of reactants in the polymer matrix was much lower than that in bulk solution, resulting in the lower conversion of TCE in membrane systems. The aggregated particles were also observed on the membrane surface which increased the diffusion resistance. If all particles are distributed uniformly like those inside the pores, we should expect a higher reaction rate and efficiency. The catalytic membranes can retain the metal ions within polymer matrix by ion exchange while maintaining the pH at near-neutral values. Figure S5 in Supplementary material shows that the iron oxide immobilized PAA/PVDF membranes still have the ion exchange capacity as the carboxyl groups stay in the membranes during the in situ synthesis of particles. As the immobilized iron oxide amount was increased by each cycle, one would expect reduction of $Fe^{2+}$ ion exchange because of mass transfer issues, and this was indeed the case.

### Reaction mechanism

The oxidative dechlorination is attributed to the reaction of $OH^{\bullet}$ with model contaminants and adsorption–desorption effect of reactants on iron oxide surfaces (Pignatello et al. 2006). The first step of TCE oxidation is considered as the fast addition of $OH^{\bullet}$ to the double bond of TCE (Kwan and Voelker 2002). It produces the intermediates which are further oxidized into organic acids and chloride by $OH^{\bullet}$. The sorption is critical in the oxidation of trace organic compounds as free radicals may only appear and react with the contaminants near the particle surfaces where they are generated (Huling and Pivetz 2006). Xue et al. reported the adsorption and oxidation of pentachlorophenol (PCP) on the surface of magnetite. The interaction between iron oxide surfaces and PCP could be expressed by the equilibrium reaction of sorbed and aqueous species (Xue et al. 2009).

At high contaminant concentrations, $OH^{\bullet}$ are mostly scavenged by the model contaminants ($k = 2$ to $5 \times 10^9$ $M^{-1}$ $s^{-1}$). At low contaminant concentrations, $OH^{\bullet}$ also reacts with $H_2O_2$ ($k = 3.3 \times 10^7$ $M^{-1}$ $s^{-1}$) due to the competitive reaction between contaminants and $H_2O_2$ near the catalytic sites. As the concentration of $H_2O_2$ increases, the reaction between $OH^{\bullet}$ and $H_2O_2$ will be enhanced. The oxidation rate of model compounds such as TCE was usually approximated by the second-order reaction mechanism at high $H_2O_2$ concentrations:

$$-\frac{dC_{TCE}}{dt} = k_1 C_{OH^\bullet} C_{TCE}, \quad (7)$$

where $C_{TCE}$ is the concentration of dissolved TCE in the solution, $C_{OH^\bullet}$ is the concentration of $OH^\bullet$ and $k_1$ is the second-order reaction rate. The pseudo-first-order kinetics [Eq. (8)] could be obtained if $C_{OH^\bullet}$ was constant at the steady-state.

$$-\frac{dC_{TCE}}{dt} = k_{obs(TCE)} C_{TCE}, \quad (8)$$

where $k_{obs(TCE)}$ is the observed pseudo-first-order reaction rate and $k_{obs(TCE)} = k_1 C_{OH^\bullet}$. While in our system, TCE concentration could not fit the pseudo-first-order approximation over the full range. The sorption had to be considered here as the concentration of $H_2O_2$ was only 0.13 % (volume) and the iron oxide loading was high (1.33 g/L). Therefore, we propose the following reaction pathway:

$$TCE + \equiv S \leftrightarrow TCE \equiv S \xrightarrow{OH^\bullet} I \xrightarrow{OH^\bullet} P + Cl^- + \equiv S, \quad (9)$$

where ≡S represents the catalytic sites on iron oxide surfaces, I is the intermediate formed during TCE oxidation, and P is the final products. The interaction of TCE and iron oxide surfaces can be expressed by the equilibrium in Eq. (9). The rate of TCE oxidation depends on the catalyst loading, the equilibrium constant for TCE adsorption, and the amount of $OH^\bullet$ generated by the reaction of $H_2O_2$ with iron oxide.

## Conclusions

The experiments using CMC-stabilized iron oxide NPs and iron oxide/PAA/PVDF membranes both illustrated their potentials for groundwater remediation at near-neutral pH values. Subsequent oxidation of iron NPs in aqueous phase resulted in amorphous ferrihydrite NPs as evidenced by XRD and Mössbauer spectroscopy. The continuous air oxidation of iron led to the growth of its specific surface area which enhanced the catalytic decomposition of $H_2O_2$. Cross-linked PAA functionalized PVDF membranes were synthesized by in situ polymerization of acrylic acid. Iron oxide NPs were successfully synthesized in the PAA/PVDF membrane pores by ion exchange, chemical reduction, and controlled oxidation. The PAA matrix prevented the agglomeration of NPs and reduced the particle loss by recapturing the metal ions. $OH^\bullet$ generated via catalytic decomposition of $H_2O_2$ reacted with TCE and $H_2O_2$ adsorbed on iron oxide surfaces simultaneously. The efficiency of systems was determined by the catalyst loading, the molar ratio of reactants and the environmental pH.

## Supplementary Material

Refer to Web version on PubMed Central for supplementary material.

## Acknowledgments

This research was supported by a joint National Institute of Environmental Health Sciences (NIEHS) SRP Supplement grant between University of Kentucky (UK) and University of California at Berkeley, UK-NIEHS-SRP program and by the US Department of Energy (DOE) KRCEE programs (DE-FG05–03OR23032). We thank Dr. Frank E. Huggins from Department of Chemical and Materials Engineering at UK for Mössbauer spectroscopy analytical support.

## References

Ahuja DK, Bachas LG, Bhattacharyya D (2007) Modified Fenton reaction for trichlorophenol dechlorination by enzymatically generated H2O2 and gluconic acid chelate. Chemosphere 66(11): 2193–2200. doi:10.1016/j.chemosphere.2006.08.035 [PubMed: 17166556]

Ai ZH, Lu LR, Li JP, Zhang LZ, Qiu JR, Wu MH (2007) Fe@$Fe_2O_3$ core–shell nanowires as iron reagent. 1. Efficient degradation of Rhodamine B by a novel sono-Fenton process. J Phys Chem C 111(11):4087–4093. doi:10.1021/Jp0655591

Bell AT (2003) The impact of nanoscience on heterogeneous catalysis. Science 299(5613):1688–1691. doi: 10.1126/science.1083671 [PubMed: 12637733]

Clapp PA, Evans DF, Sheriff TSS (1989) Spectrophotometric determination of hydrogen-peroxide after extraction with ethyl-acetate. Anal Chim Acta 218(2):331–334. doi: 10.1016/S0003-2670(00)80309-8

Costa RCC, Moura FCC, Ardisson JD, Fabris JD, Lago RM(2008) Highly active heterogeneous Fenton-like systems based on $Fe^0/Fe_3O_4$ composites prepared by controlled reduction of iron oxides. Appl Catal B 83(1–2):131–139. doi:10.1016/j.apcatb.2008.01.039

Dhananjeyan MR, Mielczarski E, Thampi KR, Buffat P, Bensimon M, Kulik A, Mielczarski J, Kiwi J (2001) Photodynamics and surface characterization of $TiO_2$ and $Fe_2O_3$ photocatalysts immobilized on modified polyethylene films. J Phys Chem B 105(48):12046–12055. doi: 10.1021/Jp011339q

Fenton HJH (1894) Oxidation of tartaric acid in presence of iron. J Chem Soc Trans 65:899–910. doi: 10.1039/CT8946500899

Furukawa Y, Kim JW, Watkins J, Wilkin RT (2002) Formation of ferrihydrite and associated iron corrosion products in permeable reactive barriers of zero-valent iron. Environ Sci Technol 36(24): 5469–5475. doi:10.1021/Es025533h [PubMed: 12521177]

Gates DD, Siegrist RL (1995) In situ chemical oxidation of trichloroethylene using hydrogen peroxide. J Environ Eng 121(9):639–644. doi:10.1061/(ASCE)0733-9372(1995)121:9(639

Giraldi TR, Arruda CC, da Costa GM, Longo E, Ribeiro C (2009) Heterogeneous Fenton reactants: a study of the behavior of iron oxide nanoparticles obtained by the polymeric precursor method. J Sol Gel Sci Technol 52(2):299–303. doi:10.1007/s10971-009-2014-2

Guo L, Huang QJ, Li XY, Yang SH (2006) PVP-coated iron nanocrystals: anhydrous synthesis, characterization, and electrocatalysis for two species. Langmuir 22(18):7867–7872. doi:10.1021/La060975i [PubMed: 16922576]

He F, Zhao DY (2008) Hydrodechlorination of trichloroethene using stabilized Fe–Pd nanoparticles: reaction mechanism and effects of stabilizers, catalysts and reaction conditions. Appl Catal B 84(3–4):533–540. doi:10.1016/j.apcatb.2008.05.008

He F, Zhao DY, Liu JC, Roberts CB (2007) Stabilization of Fe–Pd nanoparticles with sodium carboxymethyl cellulose for enhanced transport and dechlorination of trichloroethylene in soil and groundwater. Ind Eng Chem Res 46(1):29–34. doi:10.1021/Ie0610896

Hu K, Dickson JM (2007) Development and characterization of poly(vinylidene fluoride)–poly(acrylic acid) pore-filled pH-sensitive membranes. J Membr Sci 301(1–2):19–28. doi:10.1016/j.memsci.2007.05.031

Huang HH, Lu MC, Chen JN (2001) Catalytic decomposition of hydrogen peroxide and 2-chlorophenol with iron oxides. Water Res 35(9):2291–2299. doi:10.1016/S0043-1354(00)00496-6 [PubMed: 11358310]

Huling SG, Pivetz BE (2006) In situ chemical oxidation. EPA-Engineering Issue. US Environmental Protection Agency (EPA), Washington, DC

Hwang I, Kim HS, Ahn JY, Hwang KY, Kim IK (2010) Atmospherically stable nanoscale zero-valent iron particles formed under controlled air contact: characteristics and reactivity. Environ Sci Technol 44(5):1760–1766. doi: 10.1021/es902772r [PubMed: 20136088]

Kanel SR, Manning B, Charlet L, Choi H (2005) Removal of arsenic(III) from groundwater by nanoscale zero-valent iron. Environ Sci Technol 39(5):1291–1298. doi:10.1021/Es048991u [PubMed: 15787369]

Keenan CR, Sedlak DL (2008) Factors affecting the yield of oxidants from the reaction of nanoparticulate zero-valent iron and oxygen. Environ Sci Technol 42(4):1262–1267. doi:10.1021/Es7025664 [PubMed: 18351103]

Kitajima N, Fukuzumi S, Ono Y (1978) Formation of super-oxide ion during decomposition of hydrogen-peroxide on supported metal-oxides. J Phys Chem 82(13):1505–1509. doi:10.1021/j100502a009

Kwan WP, Voelker BM (2002) Decomposition of hydrogen peroxide and organic compounds in the presence of dissolved iron and ferrihydrite. Environ Sci Technol 36(7):1467–1476. doi:10.1021/Es011109p [PubMed: 11999052]

Kwan WP, Voelker BM (2003) Rates of hydroxyl radical generation and organic compound oxidation in mineral-catalyzed Fenton-like systems. Environ Sci Technol 37(6):1150–1158. doi:10.1021/Es020874g [PubMed: 12680668]

Laine DF, Cheng IF (2007) The destruction of organic pollutants under mild reaction conditions: a review. Microchem J 85(2):183–193. doi:10.1016/j.microc.2006.07.002

Lee C, Sedlak DL (2009) A novel homogeneous Fenton-like system with Fe(III)-phosphotungstate for oxidation of organic compounds at neutral pH values. J Mol Catal A 311(1–2):1–6. doi:10.1016/j.molcata.2009.07.001

Lee YN, Lago RM, Fierro JLG, Gonzalez J (2001) Hydrogen peroxide decomposition over Ln(1 - x)A(x)MnO(3) (Ln = La or Nd and A = K or Sr) perovskites. Appl Catal A 215(1–2):245–256. doi:10.1016/S0926-860X(01)00536-1

Lewis S, Lynch A, Bachas L, Hampson S, Ormsbee L, Bhattacharyya D (2009) Chelate-modified Fenton reaction for the degradation of trichloroethylene in aqueous and two-phase systems. Environ Eng Sci 26(4):849–859. doi:10.1089/ees.2008.0277 [PubMed: 20418966]

Lewis SR, Datta S, Gui M, Coker EL, Huggins FE, Daunert S, Bachas L, Bhattacharyya D (2011) Reactive nanostructured membranes for water purification. Proc Natl Acad Sci USA 108(21):8577–8582. doi:10.1073/pnas.1101144108 [PubMed: 21606340]

Li K, Stefan MI, Crittenden JC (2007a) Trichloroethene degradation by UV/$H_2O_2$ advanced oxidation process: product study and kinetic modeling. Environ Sci Technol 41(5): 1696–1703. doi:10.1021/Es0607638 [PubMed: 17396662]

Li YC, Bachas LG, Bhattacharyya D (2007b) Selected chloro-organic detoxifications by polychelate (poly(acrylic acid)) and citrate-based Fenton reaction at neutral pH environment. Ind Eng Chem Res 46(24):7984–7992. doi:10.1021/Ie070393b

Lim H, Lee J, Jin S, Kim J, Yoon J, Hyeon T (2006) Highly active heterogeneous Fenton catalyst using iron oxide nanoparticles immobilized in alumina coated mesoporous silica. Chem Commun 4:463–465. doi:10.1039/B513517f

Lin SS, Gurol MD (1998) Catalytic decomposition of hydrogen peroxide on iron oxide: kinetics, mechanism, and implications. Environ Sci Technol 32(10):1417–1423. doi: 10.1021/es970648k

Miller CM, Valentine RL (1995) Hydrogen peroxide decomposition and quinoline degradation in the presence of aquifer material. Water Res 29(10):2353–2359. doi: 10.1016/0043-1354(95)00059-T

Miller CM, Valentine RL (1999) Mechanistic studies of surface catalyzed $H_2O_2$ decomposition and contaminant degradation in the presence of sand. Water Res 33(12):2805–2816. doi:10.1016/S0043-1354(98)00500-4

Nurmi JT, Tratnyek PG, Sarathy V, Baer DR, Amonette JE, Pecher K, Wang CM, Linehan JC, Matson DW, Penn RL, Driessen MD (2005) Characterization and properties of metallic iron nanoparticles: spectroscopy, electrochemistry, and kinetics. Environ Sci Technol 39(5):1221–1230. doi:10.1021/Es049190u [PubMed: 15787360]

Peng S, Wang C, Xie J, Sun SH (2006) Synthesis and stabilization of monodisperse Fe nanoparticles. J Am Chem Soc 128(33):10676–10677. doi:10.1021/Ja063969h [PubMed: 16910651]

Pham ALT, Lee C, Doyle FM, Sedlak DL (2009) A silica-supported iron oxide catalyst capable of activating hydrogen peroxide at neutral pH values. Environ Sci Technol 43(23):8930–8935. doi:10.1021/Es902296k [PubMed: 19943668]

Pignatello JJ, Oliveros E, MacKay A (2006) Advanced oxidation processes for organic contaminant destruction based on the Fenton reaction and related chemistry. Crit Rev Environ Sci Technol 36(1):1–84. doi:10.1080/10643380500326564

Ravikumar JX, Gurol MD (1994) Chemical oxidation of chlorinated organics by hydrogen-peroxide in the presence of sand. Environ Sci Technol 28(3):394–400. doi:10.1021/es00052a009 [PubMed: 22165872]

Saleh AM, Jones AA (1984) The crystallinity and surface characteristics of synthetic ferrihydrite and its relationship to kaolinite surfaces. Clay Miner 19(5):745–755. doi: 10.1180/claymin.1984.019.5.05

Savage N, Diallo MS (2005) Nanomaterials and water purification: opportunities and challenges. J Nanopart Res 7(4–5):331–342. doi:10.1007/s11051-005-7523-5

Schwertmann U, Fechter H (1982) The point of zero charge of natural and synthetic ferrihydrites and its relation to adsorbed silicate. Clay Miner 17(4):471–476. doi:10.1180/claymin.1982.017.4.10

Singh N, Wang J, Ulbricht M, Wickramasinghe SR, Husson SM (2008) Surface-initiated atom transfer radical polymerization: a new method for preparation of polymeric membrane adsorbers. J Membr Sci 309(1–2):64–72. doi: 10.1016/j.memsci.2007.10.007

Smuleac V, Bachas L, Bhattacharyya D (2010) Aqueous-phase synthesis of PAA in PVDF membrane pores for nanoparticle synthesis and dichlorobiphenyl degradation. J Membr Sci 346(2):310–317. doi:10.1016/j.memsci.2009.09.052

Sun SP, Lemley AT (2011) p-Nitrophenol degradation by a heterogeneous Fenton-like reaction on nano-magnetite: process optimization, kinetics, and degradation pathways. J Mol Catal A 349(1–2):71–79. doi:10.1016/j.molcata.2011.08.022

Tee YH, Bachas L, Bhattacharyya D (2009) Degradation of trichloroethylene and dichlorobiphenyls by iron-based bimetallic nanoparticles. J Phys Chem C 113(22): 9454–9464. doi:10.1021/Jp809098z

Tratnyek PG, Johnson RL (2006) Nanotechnologies for environmental cleanup. Nano Today 1(2):44–48

Tyre BW, Watts RJ, Miller GC (1991) Treatment of 4 biorefractory contaminants in soils using catalyzed hydrogen peroxide. J Environ Qual 20(4):832–838. doi:10.2134/jeq1991.00472425002000040021x

Valentine RL, Wang HCA (1998) Iron oxide surface catalyzed oxidation of quinoline by hydrogen peroxide. J Environ Eng 124(1):31–38. doi:10.1061/(ASCE)0733-9372(1998)124:1(31

Voinov MA, Pagan JOS, Morrison E, Smirnova TI, Smirnov AI (2011) Surface-mediated production of hydroxyl radicals as a mechanism of iron oxide nanoparticle biotoxicity. J Am Chem Soc 133(1):35–41. doi:10.1021/Ja104683w [PubMed: 21141957]

Wang CB, Zhang WX (1997) Synthesizing nanoscale iron particles for rapid and complete dechlorination of TCE and PCBs. Environ Sci Technol 31(7):2154–2156. doi: 10.1021/es970039c

Wang F, Chen TL, Xu JP (1998) Sodium sulfonate-functionalized poly(ether ether ketone)s. Macromol Chem Phys 199(7):1421–1426. doi:10.1002/(SICI)1521-3935(19980701)199:7

Watts RJ, Teel AL (2005) Chemistry of modified Fenton's reagent (catalyzed H2O2 propagations-CHP) for in situ soil and groundwater remediation. J Environ Eng 131(4): 612–622. doi:10.1061/(Asce)0733-9372(2005)131:4(612

Watts RJ, Udell MD, Kong SH, Leung SW (1999) Fenton-like soil remediation catalyzed by naturally occurring iron minerals. Environ Eng Sci 16(1):93–103. doi:10.1089/ees.1999.16.93

Wycisk R, Pintauro PN (1996) Sulfonated polyphosphazene ion-exchange membranes. J Membr Sci 119(1):155–160. doi:10.1016/0376-7388(96)00146-9

Xu J, Bhattacharyya D (2007) Fe/Pd nanoparticle immobilization in microfiltration membrane pores: synthesis, characterization, and application in the dechlorination of polychlorinated biphenyls. Ind Eng Chem Res 46(8): 2348–2359. doi:10.1021/Ie0611498

Xu J, Bhattacharyya D (2008) Modeling of Fe/Pd nanoparticle-based functionalized membrane reactor for PCB dechlori-nation at room temperature. J Phys Chem C 112(25): 9133–9144. doi:10.1021/Jp7097262

Xu J, Dozier A, Bhattacharyya D (2005) Synthesis of nanoscale bimetallic particles in polyelectrolyte membrane matrix for reductive transformation of halogenated organic compounds. J Nanopart Res 7(4–5):449–467. doi:10.1007/s11051-005-4273-3

Xue XF, Hanna K, Abdelmoula M, Deng NS (2009) Adsorption and oxidation of PCP on the surface of magnetite: kinetic experiments and spectroscopic investigations. Appl Catal B 89(3–4):432–440. doi:10.1016/j.apcatb.2008.12.024

Yeh CK-J, Chen W-S, Chen W-Y (2004) Production of hydro-xyl radicals from the decomposition of hydrogen peroxide catalyzed by various iron oxides at pH 7. Pract Period Hazard Toxic Radioact Waste Manag 8(3):161–165. doi:10.1061/(ASCE)1090-025X(2004)8:3(161

Zelmanov G, Semiat R (2008) Iron(3) oxide-based nanoparticles as catalysts in advanced organic aqueous oxidation. Water Res 42(1–2):492–498. doi:10.1016/j.watres.2007.07.045 [PubMed: 17714754]

Zhang WX (2003) Nanoscale iron particles for environmental remediation: an overview. J Nanopart Res 5(3–4):323–332. doi:10.1023/A:1025520116015

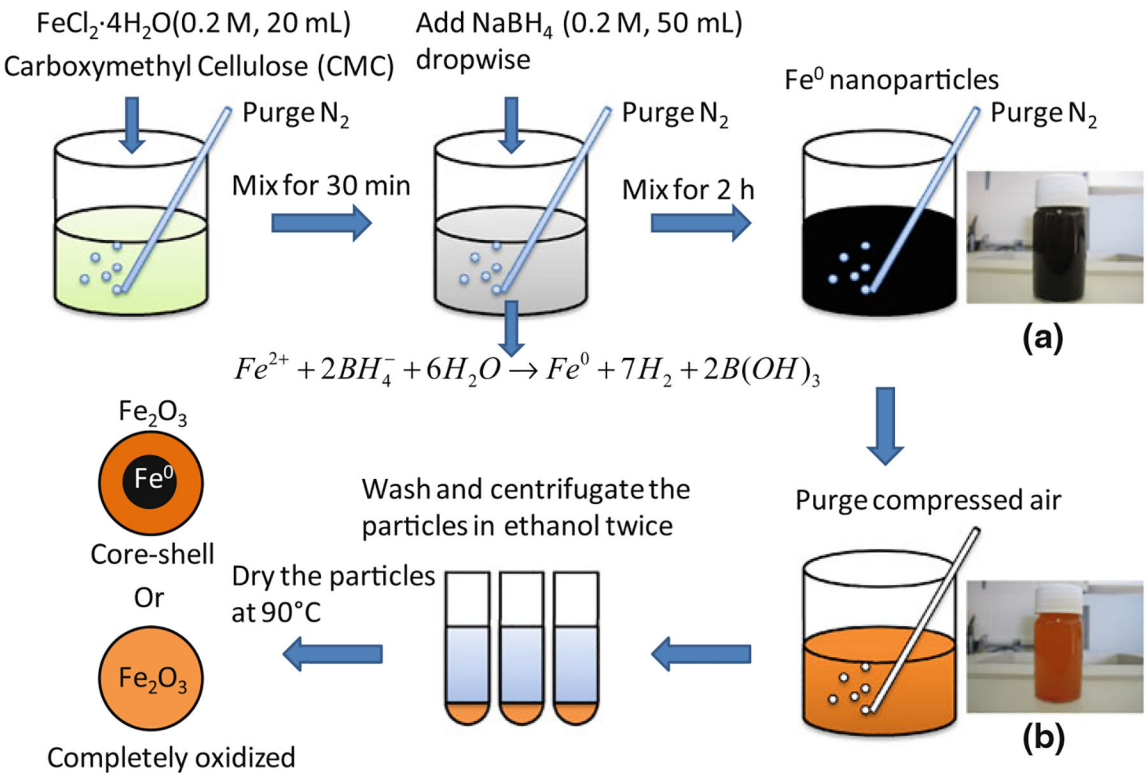


**Fig. 1.**

Schematic of CMC-stabilized iron and iron oxide NP synthesis: **a** $Fe^0$ NPs, **b** iron/iron oxide NPs synthesized by air oxidation of $Fe^0$ NPs

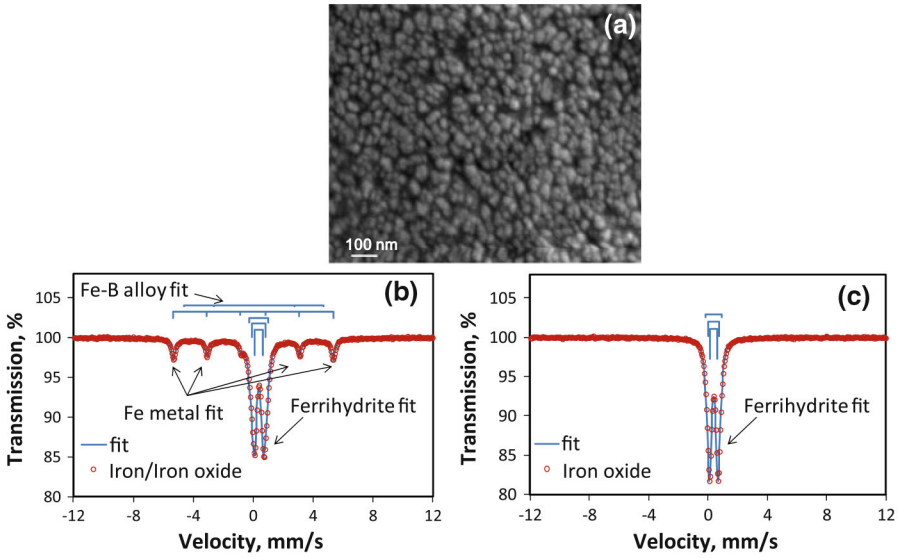


**Fig. 2.**

Iron oxide NPs synthesized by air oxidation of $Fe^0$ NPs for 1 h. **a** SEM image of iron oxide, **b** $^{57}Fe$ Mössbauer spectrum of iron/iron oxide core–shell NPs before oxidation, and **c** $^{57}Fe$ Mössbauer spectrum of iron oxide

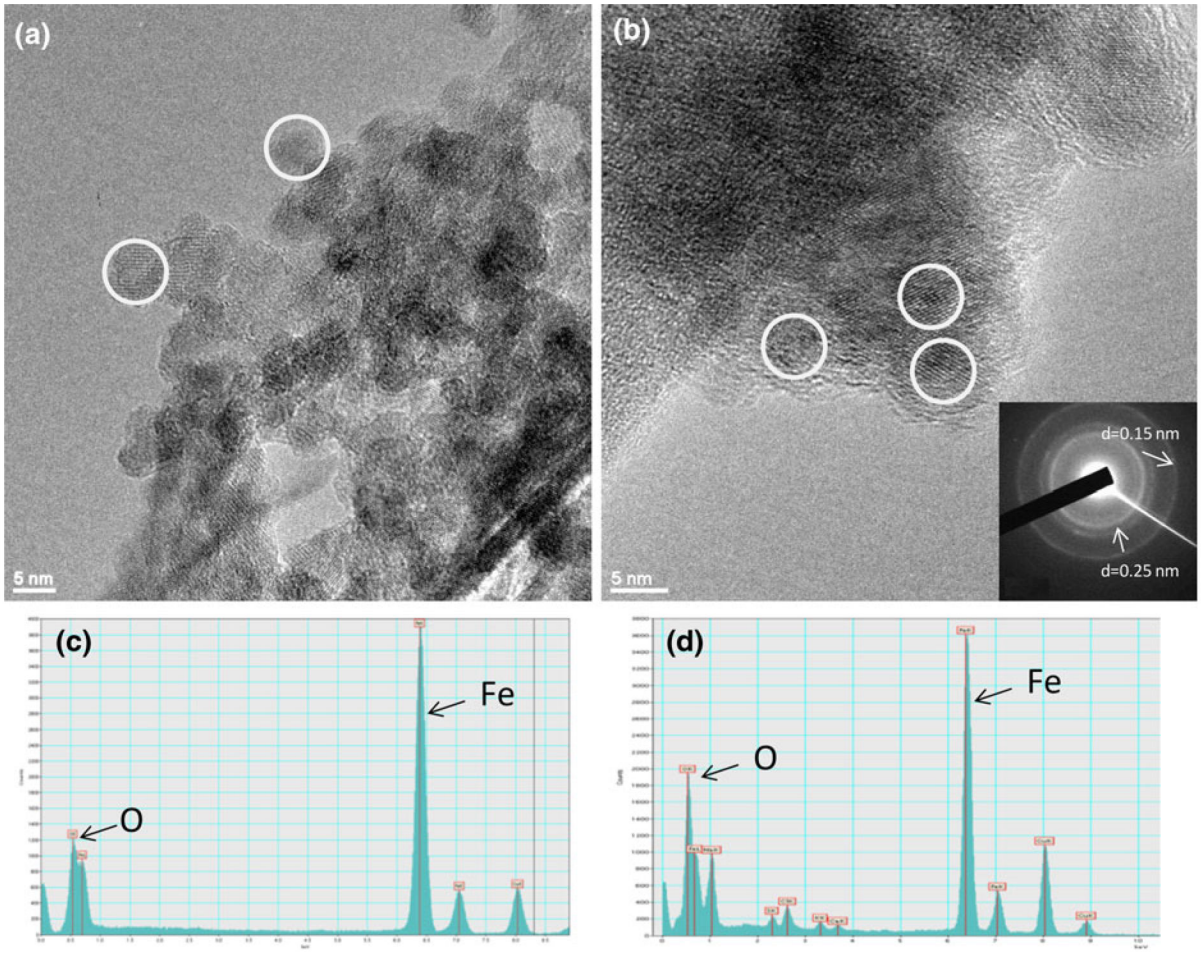


**Fig. 3.**

HRTEM images and EDX spectra of iron (**a, c**) and iron oxide NPs (**b, d**). SAED pattern (*inset* of **b**) corresponds to (110) and (300) of ferrihydrite. *White circles* indicate the iron and iron oxide NPs

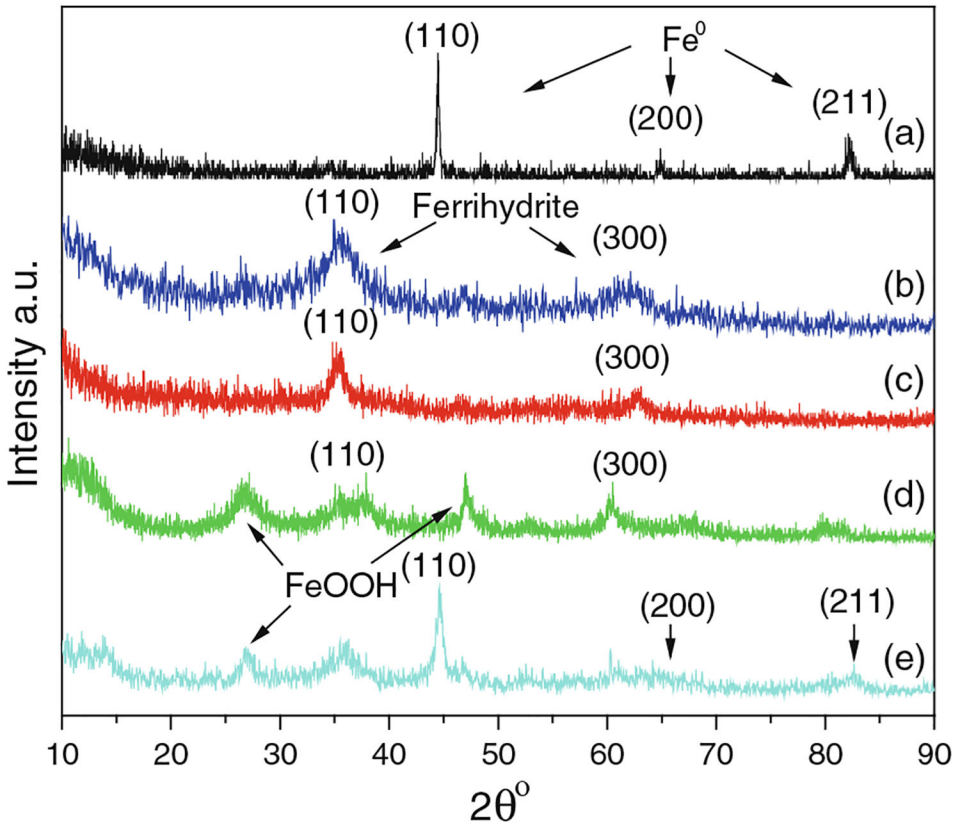


**Fig. 4.**

XRD spectra of fresh iron NPs (*a*), iron oxide NPs synthesized by air oxidation of $Fe^0$ for: (*b*) 0.25 h, (*c*) 0.5 h, (*d*) 1 h, and aged iron NPs (*e*). The peaks shown in diffraction patterns correspond as follows: for (*a*) and (*e*), Miller indices (110), (200), and (211) of a-Fe (Powder Diffraction File No., PDF#: 00-006-0696); for (*b*), (*c*), and (*e*), Miller indices (110) and (300) of ferrihydrite (PDF#: 01-073-8408). For the rest of the peaks, other iron oxides such as, lepidocrocite (PDF#: 00-003-0079) and wustite (PDF#: 00-006-0615)

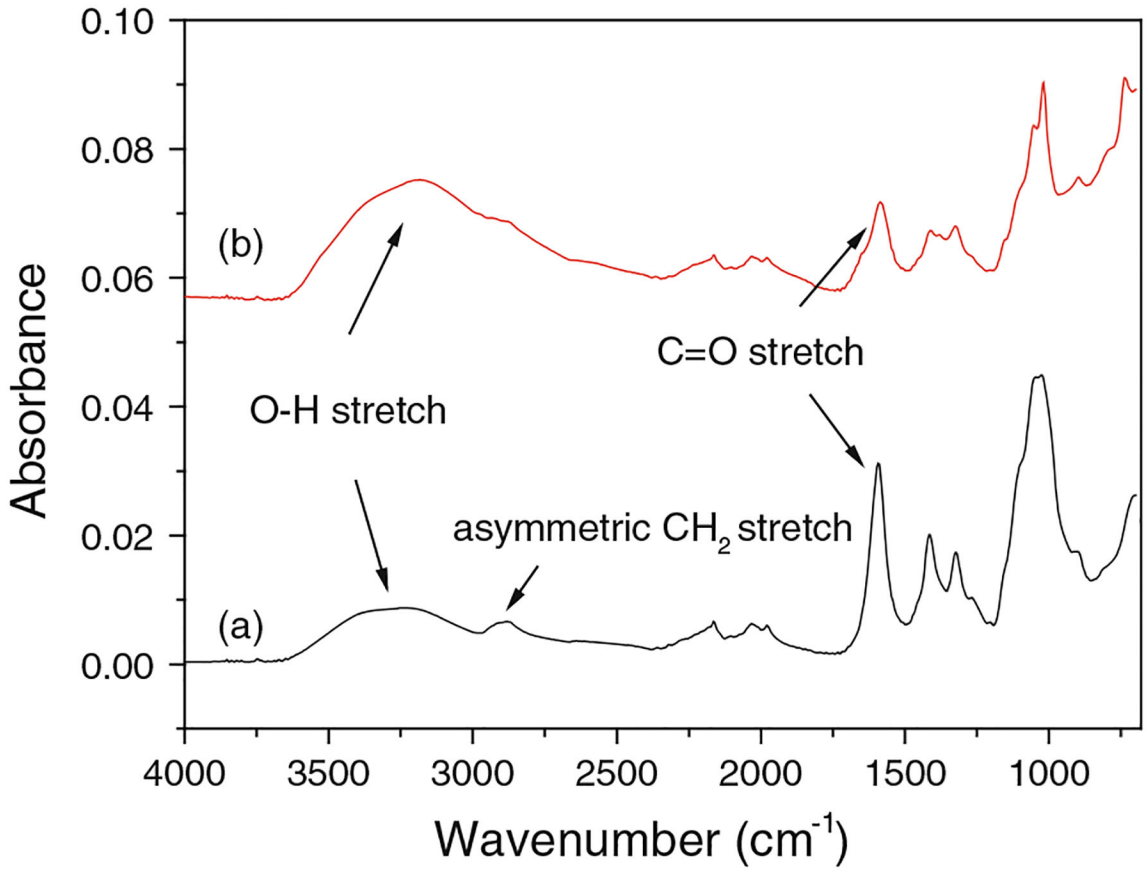


**Fig. 5.**
ATR–FTIR spectra of (*a*) pure CMC and (*b*) CMC-stabilized iron oxide NPs

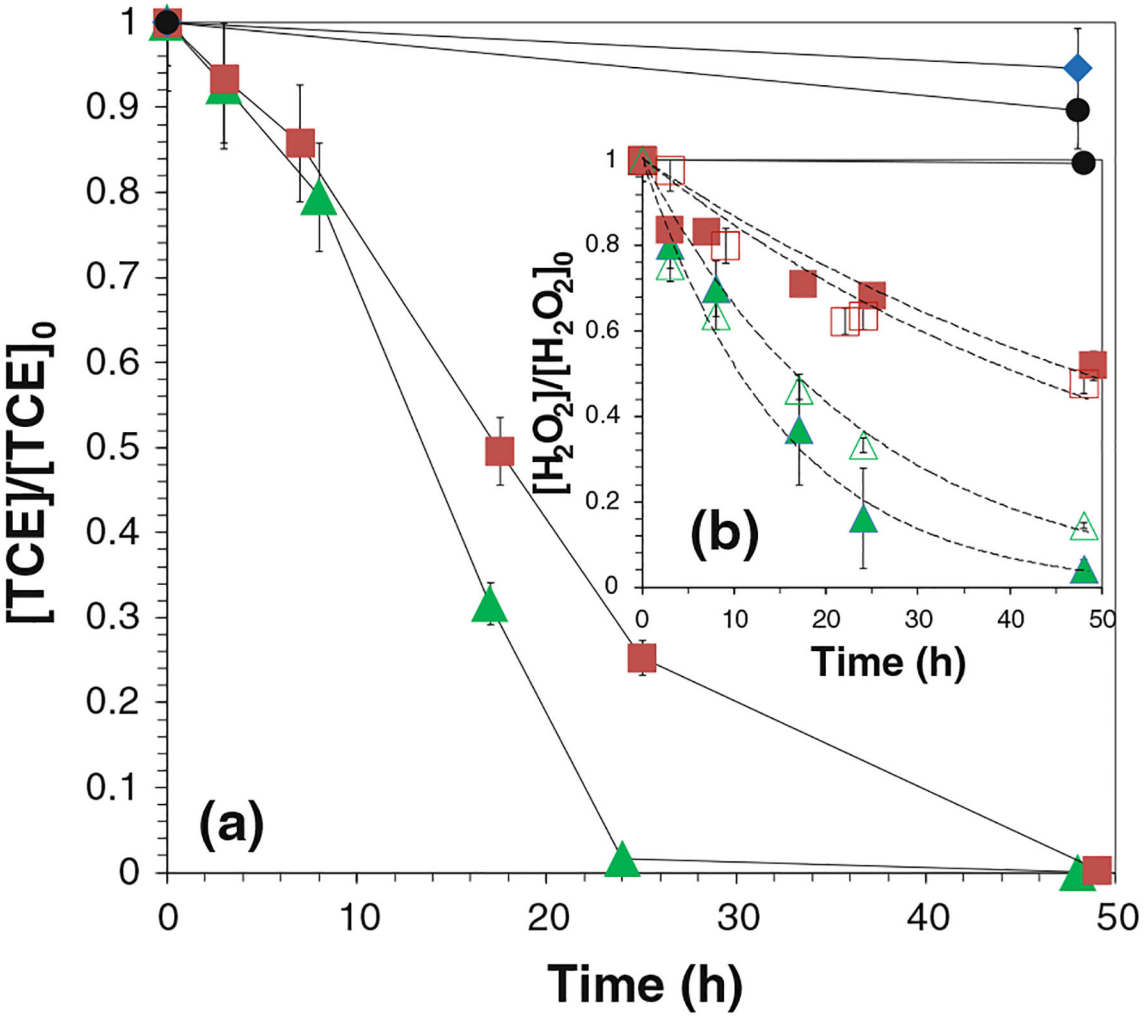


**Fig. 6.**

TCE and $H_2O_2$ decay in the iron oxide/$H_2O_2$ system. **a** The oxidation of TCE, **b** the decomposition of $H_2O_2$ in the absence (*hollow symbols*) and the presence (*solid symbols*) of TCE and the pseudo-first-order approximation by Eq. 4 (*dashed lines*). $[TCE]_0$ = 0.270 mM, $[H_2O_2]_0$ = 41.4 mM, total volume $V$ = 20 mL. pH 6.95 at $t$ = 0 and pH 4.6 at $t$ = 48 h. *Filled triangle* [iron oxide] = 1.33 g/L, *filled square* [iron oxide] = 0.67 g/L, *filled diamond control* (iron oxide in TCE solution), *filled circle control* (TCE and $H_2O_2$ solution), *open triangle* [iron oxide] = 1.33 g/L, open square [iron oxide] = 0.67 g/L

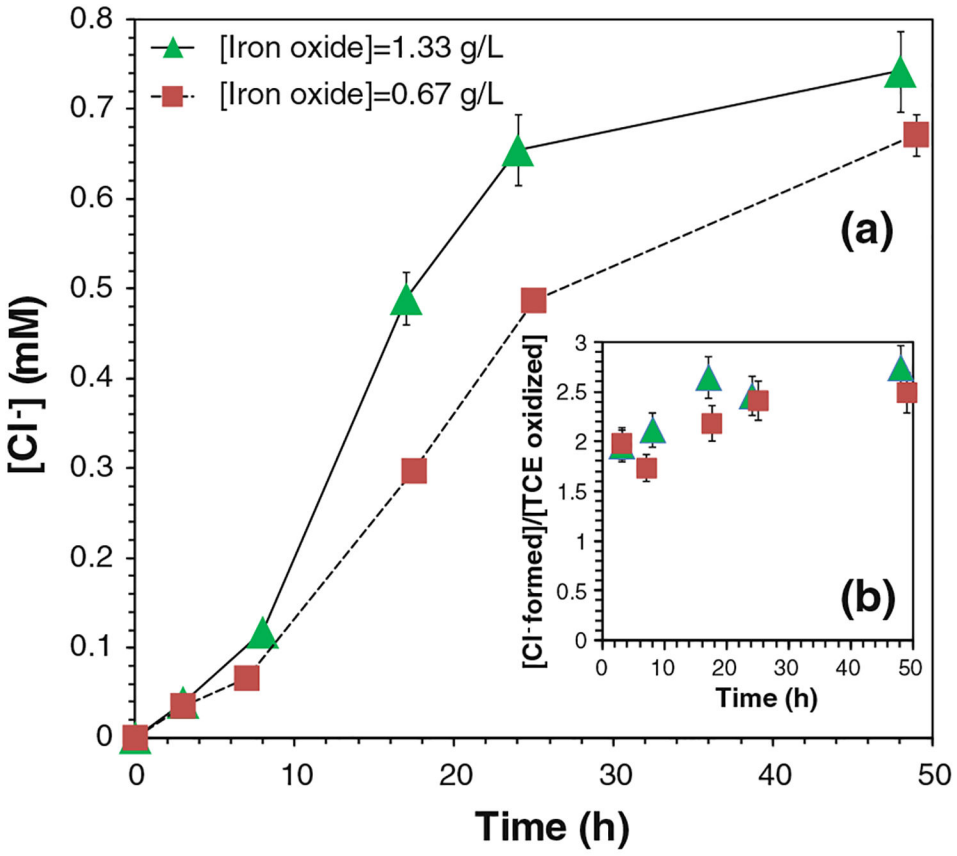


**Fig. 7.**

Chloride ($Cl^-$) formation in the iron oxide/$H_2O_2$ system. **a** The concentrations of $Cl^-$ (mM) in the reaction, b $Cl^-$ formed per TCE degraded or (mmol $Cl^-$ formed)/(mmol TCE degraded). $[TCE]_0$ = 0.270 mM, $[H_2O_2]_0$ = 41.4 mM, total volume $V$ = 20 mL. pH 6.95 at $t$ = 0 and pH 4.60 at $t$ = 48 h. For complete TCE dechlorination, $([Cl^-$ formed]/[TCE oxidized])$_{max}$ = 3

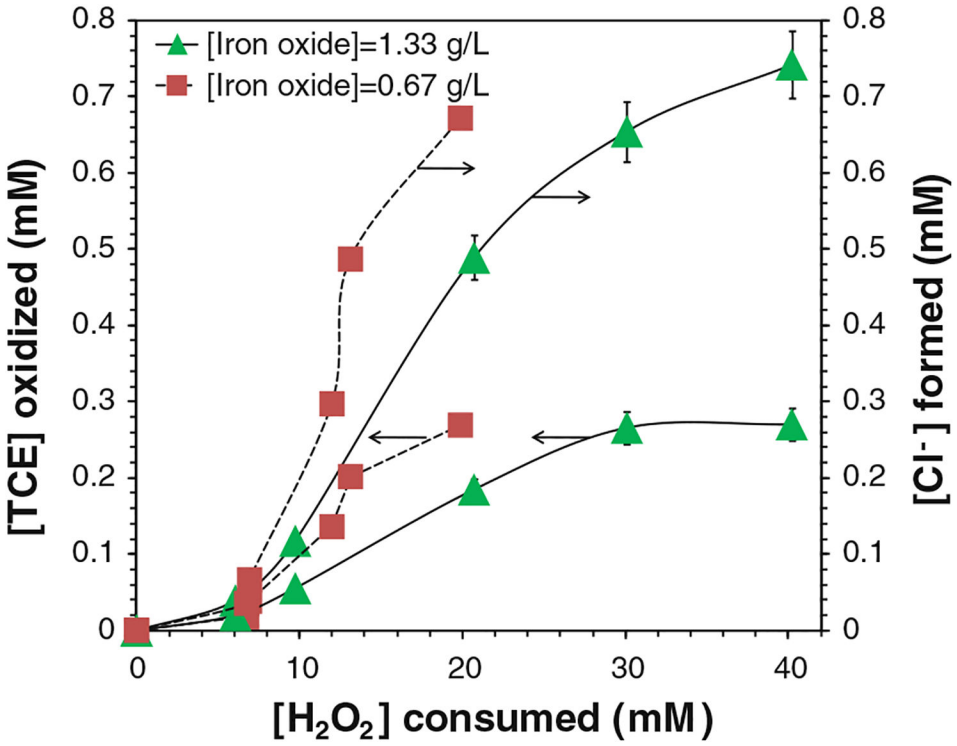


**Fig. 8.**

TCE decay and chloride ($Cl^-$) formation with $H_2O_2$ consumption in the iron oxide/$H_2O_2$ system. $[TCE]_0$ = 0.270 mM, $[H_2O_2]_0$ = 41.4 mM, total volume $V$ = 20 mL. pH 6.95 at $t$ = 0 and pH 4.6 at $t$ = 48 h. $[Cl^-\ formed]_{max}$ = 0.810 mM

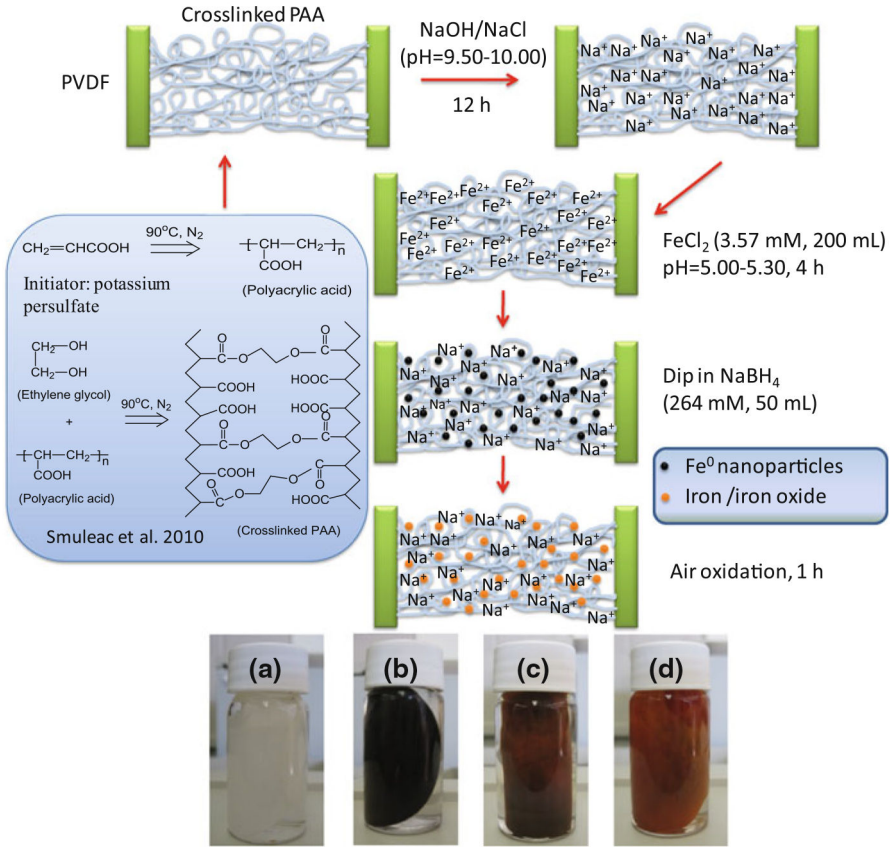


**Fig. 9.**

Schematic of preparing iron oxide/PAA/PVDF membranes (*above*) and the photos (*below*). **a** PAA/PVDF membranes, **b** $Fe^0$/PAA/PVDF membranes, **c** iron oxide/PAA/PVDF membranes prepared by air oxidation of $Fe^0$/PAA/PVDF for 1 h, and **d** iron oxide/PAA/PVDF membranes after TCE oxidation

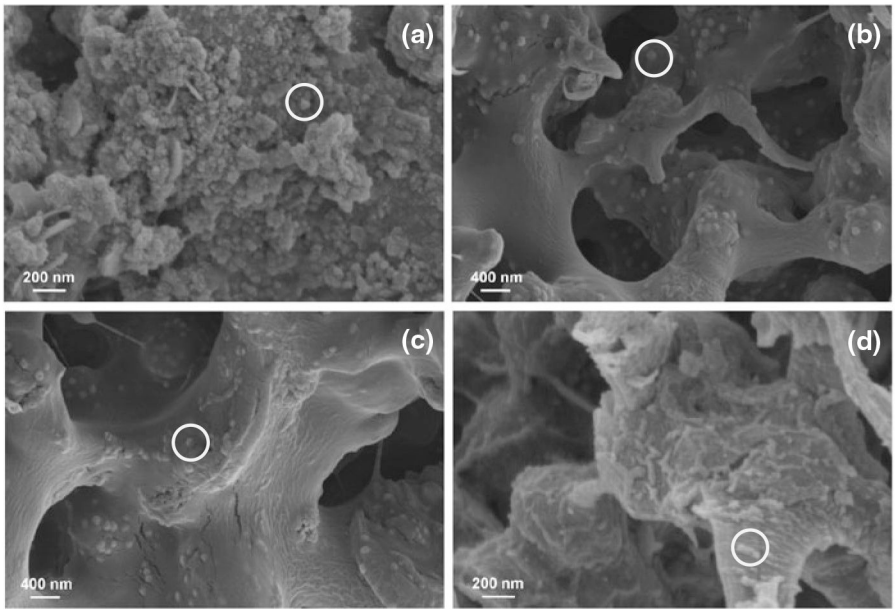


**Fig. 10.**

SEM images of iron and iron oxide/PAA/PVDF membranes: **a** membrane surface, **b** iron/PAA/PVDF (cross section), **c** iron oxide/PAA/PVDF (cross section), **d** iron oxide/PAA/PVDF after TCE oxidation (48 h, cross section). *White circles* The NPs

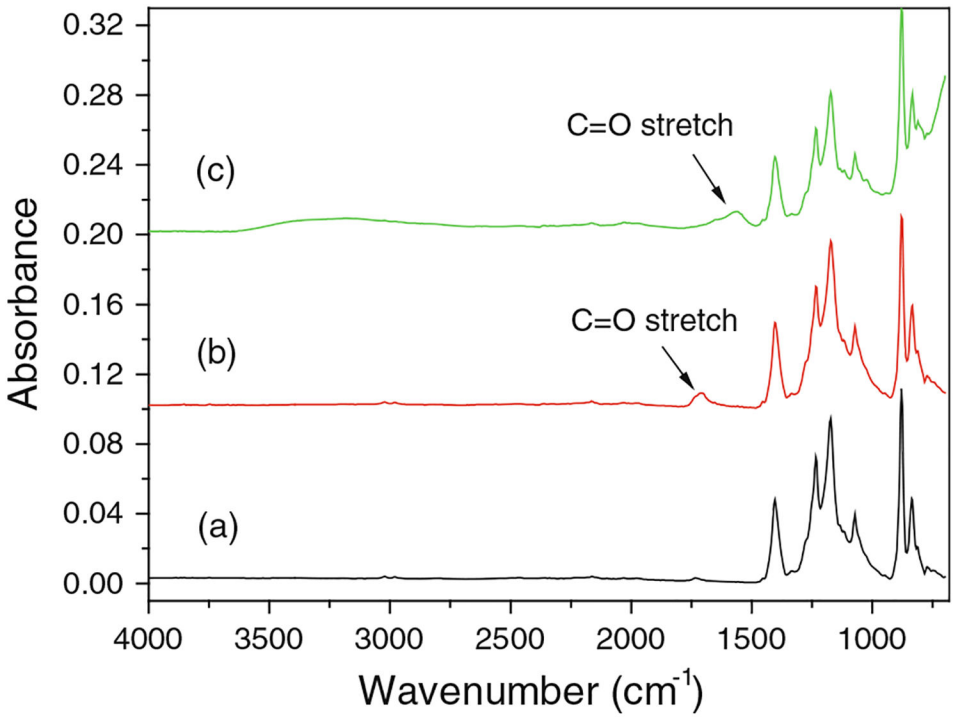


**Fig. 11.**

ATR-FTIR spectra of (*a*) bare hydrophilized PVDF membranes, (*b*) PAA functionalized PVDF membranes, and (*c*) iron oxide/PAA/PVDF membranes

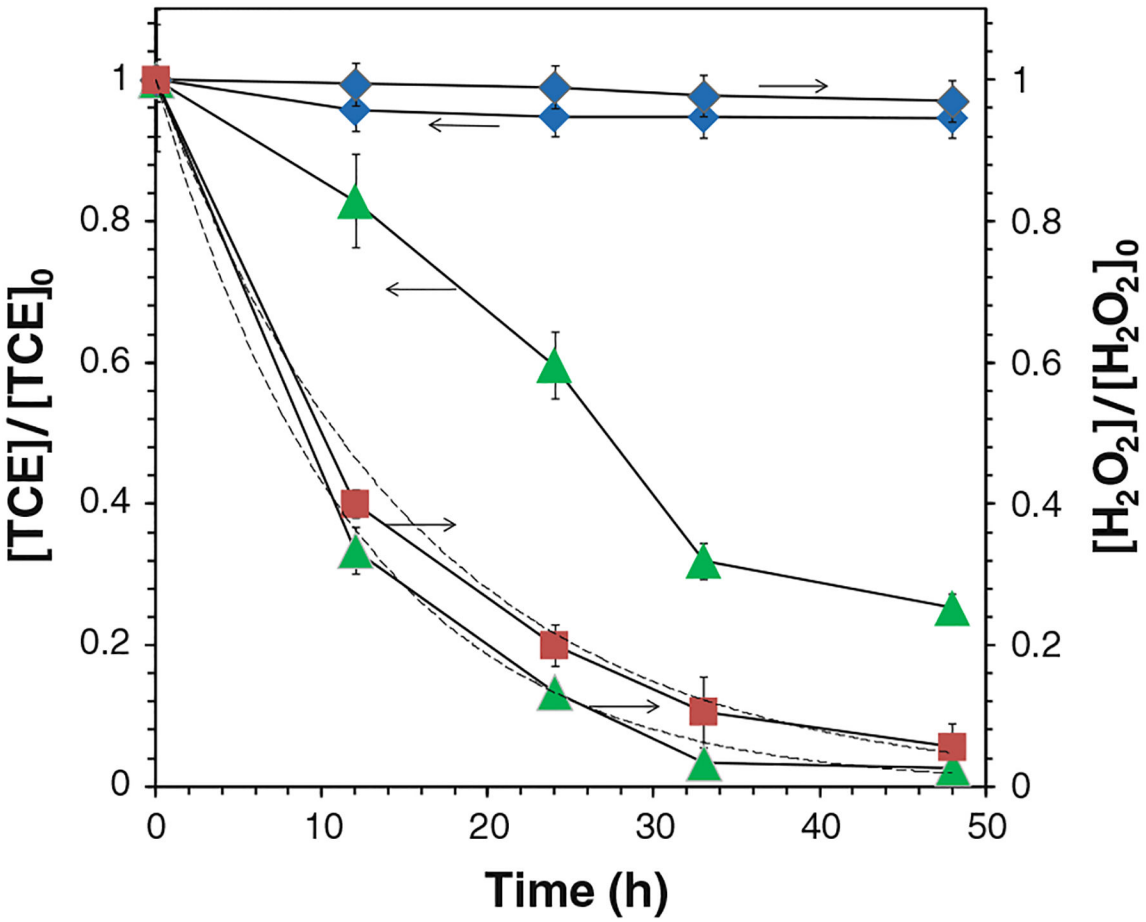


**Fig. 12.**

TCE and $H_2O_2$ decay in the iron oxide/PAA/PVDF membrane system (*solid line*). *Dash lines* The pseudo-first-order model of $H_2O_2$ decomposition [Eq. (4)]. [Total iron loading as iron oxide] = 0.88 g/L, $[TCE]_0$ = 0.270 mM, $[H_2O_2]_0$ = 41.4 mM, total volume $V$ = 20 mL. pH 7 at $t$ = 0 and pH 6.8 at $t$ = 48 h. *Filled triangle* Iron oxide/PAA/PVDF, *filled diamond control* (PAA/PVDF), *filled square control* ($H_2O_2$ decay in the absence of TCE). A small amount of TCE was extracted by PAA–PVDF membranes during the reaction (about 0.04 mM after 48 h). The data used in this figure has been modified to eliminate the extraction effect

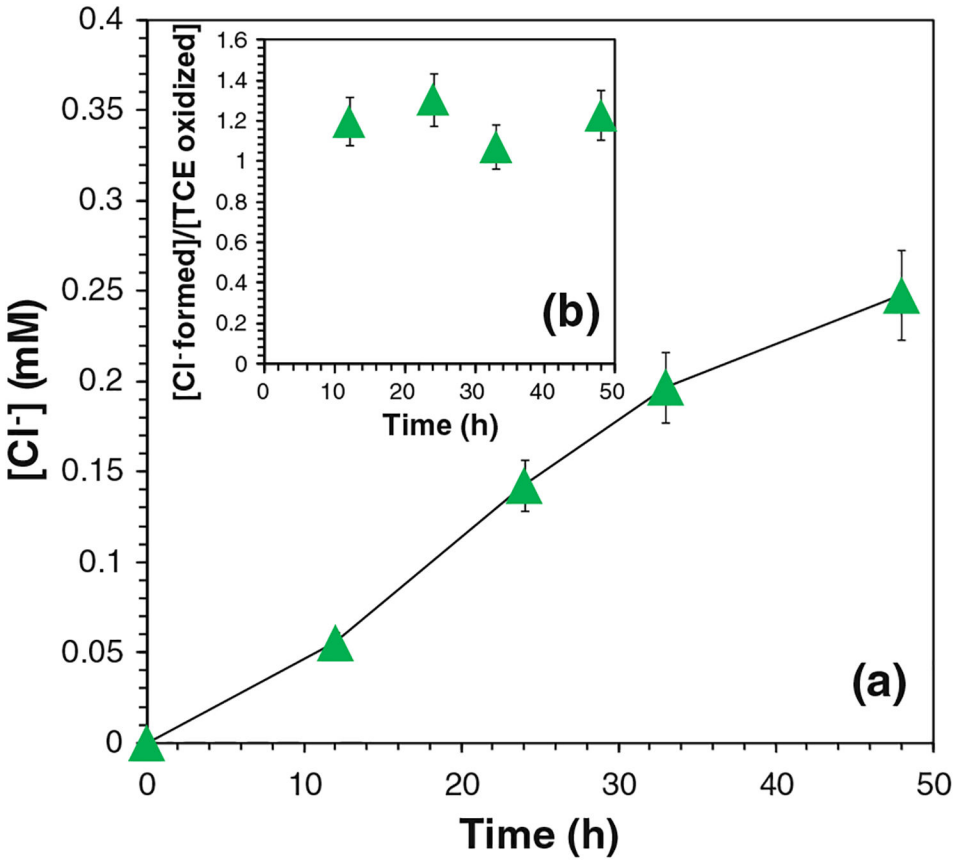


**Fig. 13.**

Chloride ($Cl^-$) formation in the iron oxide/PAA/PVDF membrane system. **a** The concentrations of $Cl^-$ (mM) in the reaction, **b** $Cl^-$ formed per TCE degraded or (mmol $Cl^-$ formed)/(mmol TCE degraded). [Total iron loading as iron oxide] = 0.88 g/L, $[TCE]_0$ = 0.270 mM, $[H_2O_2]_0$ = 41.4 mM, total volume $V$ = 20 mL. pH 7 at $t$ = 0 and pH 6.8 at $t$ = 48 h. $([Cl^- \text{ formed}]/[\text{TCE oxidized}])_{max}$ = 3

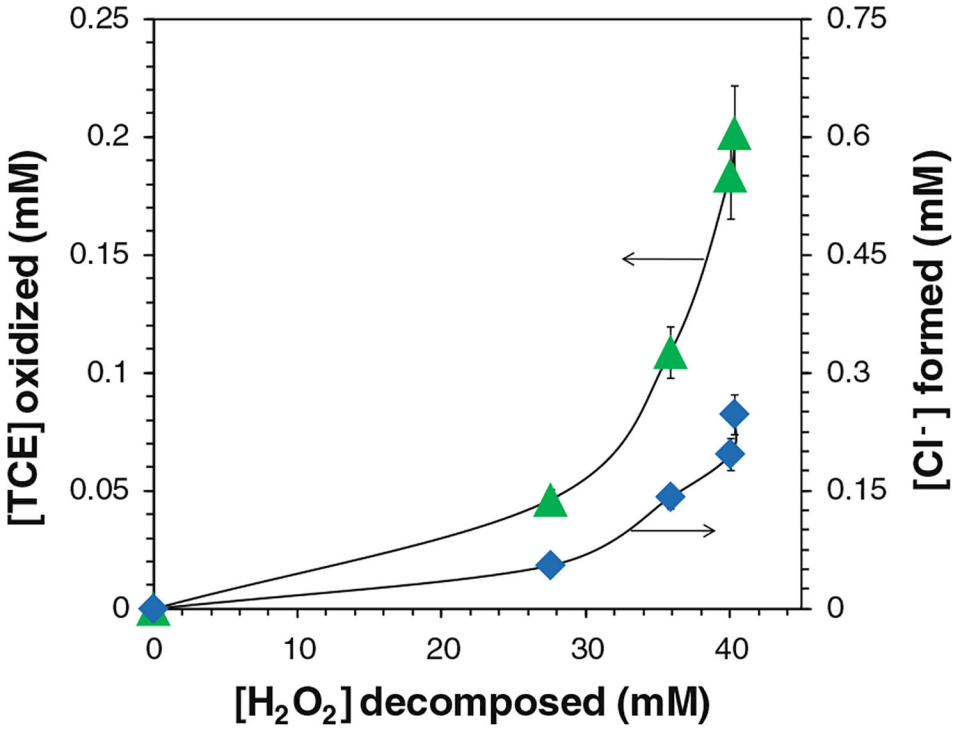


**Fig. 14.**

Relationship of TCE decay and chloride formation with $H_2O_2$ consumption in the iron oxide/PAA/PVDF membrane system. [Total iron loading as iron oxide] = 0.88 g/L, $[TCE]_0$ = 0.270 mM, $[H_2O_2]_0$ = 41.4 mM, total volume $V$ = 20 mL. pH 7 at $t$ = 0 and pH 6.8 at $t$ = 48 h. $[Cl^-formed]_{max}$ = 0.810 mM